InGaAs-Based Devices for Laser Spot Tracking and Long-Range Remote Sensing

Krishna Linga*[a], Michael Evans[a], Wei Huang[a], Paul Bereznycky[a], Scott Endicter[a], William Gustus[a], John Tagle[a], John Liobe[b]

[a]Sensors Unlimited, a Raytheon Company, 330 Carter Rd., Princeton, NJ 08540; [b]Unaffiliated

ABSTRACT

Sensors Unlimited, Inc. (SUI), a Raytheon Technologies company, presents additions to its photo-detector portfolio enabled by recent advancements in its on-site foundry capabilities. SUI has historically offered 1-D arrays of lattice-mismatched InGaAs/InP detectors alongside its lattice-matched 1-D and 2-D arrays. The use of lattice-mismatched InGaAs expands its wavelength response into the extended short-wave infrared (eSWIR) region between 1.7 µm and 2.6 µm[1][2]. SUI demonstrates herein the fabrication and testing of new 2-D eSWIR focal plane arrays (FPAs) for laser spot tracking applications, making use of its existing 640 x 512 format, 15 µm pitch, multi-mode readout integrated circuits (ROICs) and camera electronics[3]. Sample imagery and relevant spot-tracking performance metrics are discussed. Recent detector development also includes the design, processing, packaging, and testing of novel, small-pitch, SWIR avalanche photodiodes (APDs). Both Geiger and linear mode device data are presented in comparison to results predicted by TCAD simulations[4]. Parameters including noise, sensitivity, and response time are examined in the context of suitability for remote sensing and laser spot-tracking applications where long-range capability is prioritized. Pathways to integration of the new eSWIR arrays and the small-pitch SWIR APDs into larger imaging and/or laser tracking systems are explored.

INTRODUCTION

LIDAR (Light Detection and Ranging) has traditionally been used for long-range measurement applications in which accuracies of a meters or millimeters are needed[5]. The performance of the laser-based pulsed time-of-flight (TOF) range finding technique has improved during the last few years, and many new applications have opened for this method, giving new life to a well-known technology.

The noncontact operating principle, high speed measurements, sufficient resolution and millimeter accuracy when measuring distances from natural targets at long distances away, make it possible to use diode laser-based pulsed TOF rangefinders in military and civilian applications.

Short-wave infrared (SWIR) FPAs have demonstrated in-pixel multi-modal capabilities[6, 7, 8]. One such mode of operation is range finding or time-of-flight. High resolution range finding is increasingly becoming vital functionality in high precision targeting systems. The precision and accuracy of range-to-target information is an essential performance parameter of these systems. With the recent advances in LADAR (Laser Detection and Ranging) technology and sensors, range measurement accuracies as small as a centimeter have become realizable. These tracking systems are designed for long-range applications in an outdoor environment. Recent advancements include the introduction of eSWIR P-i-N detectors[9] to enable detection capabilities at wavelengths out to 2.5 microns, and the incorporation of avalanche photodiodes[10][11] (APDs), which offer additional sensitivity for long range improvement.

This paper presents the 2-D SWIR and eSWIR FPA sensor based MMT camera for accurate pulse detection, tracking, and TOF range finding technique on each pixel of the FPA. Preliminary simulation results of an eSWIR APD are presented as an initial step toward the next generation of multi-mode tracking (MMT) products.

*krishna.linga@collins.com; phone 1 609 333 8202, https://www.sensorsinc.com

Infrared Technology and Applications LI, edited by Gabor F. Fulop, Michael H. MacDougal, David Z. Ting,
Masafumi Kimata, Proc. of SPIE Vol. 13469, 134690A · 2025 Published by SPIE
0277-786X · doi: 10.1117/12.3053729

Significant progress in SWIR multi-mode pulse tracking technology includes innovation in fast pulse tracking, higher sensitivity, simultaneous multi-pulse detection & tracking, novel algorithms to accurately predict the range with high resolution and high precision and longer range and having an internal gain sensor pixel using APD technology. In addition, recent developments include pulse detection, decoding, and tracking at extended SWIR wavelength (2.0 µm) for covert and highly sensitive military applications. SUI's multi-mode tracking (MMT) technology can track moving targets under challenging conditions where a single-mode system will fail. The algorithm-based back-end processing included in SUI's MMT technology can adjust to changes in the environment such as varying light conditions, weather (fog, rain), and countermeasures to maintain maximum detection and tracking performance. MMT's versatility has made it a preferred choice for applications like border security, surveillance, and industrial automation, where robust and adaptable solutions are critical.

SUI's MMT technology has undergone significant transformations since its inception. Each new version introduced substantial improvements in detection range, resolution, and power efficiency, aligning with the evolving needs of the market. Developmental milestones of SUI's MMT technology are listed in Table 1.

Year	**Version**	**Features**
2017	MMT v1.0	Low-noise NIR-SWIR imaging and laser pulse detection at every pixel [640x512,15 µm pitch]
2019	MMT v2.0	Lower SWaP; embedded LRF receiver [1280x1024, 12 µm pitch]
2021	MMT v3.0	Lower SWaP [640x512, 15 µm pitch]
2024	MMT v4.0	High-resolution [<10 cm] ToF at every pixel [640x512, 15 µm pitch]
2026	MMT eSWIR	640x512, 15 µm pitch, 2.2 µm cut-off wavelength
2027	MMT v5.0	Up to 2kx2k, 10 µm pitch, ToF at every pixel, long range [>3km], high resolution

Table 1. MMT technology development milestones

A summary of SUI's next generation of SWIR/eSWIR, long-range, high-resolution pulse detection and tracking sensor technology under development is given in Table 2:

Mode/Feature	SUI SWIR Next-Gen	State-of-the-Art
Pixel Pitch	<10 µm	10-12 µm
Imaging Frame Rate	≥120 FPS	60-120 FPS
Dynamic Range	≥1900:1	~1000:1
Noise Level	≤10 e-	5-10 e-
ALPD Frame Rate	≤50 kHz	10-20 kHz
ALPD Sensitivity	≤1000 e-	~1500-3000 e-
ToF Depth Accuracy	≤1 cm	~2-5 cm
ToF Range	≥ 3000 m	≤250 m

Table 2. Pulse detection and tracking development.

SWIR Avalanche Photodiode and Excess Noise Factor

InP-based avalanche photodiodes (APDs) are attractive for use in laser range finding and tracking, photon detection, and low light level imaging applications due to their internal gain. Their sensitivity is ultimately limited by multiplication noise due to the inherent statistical nature of the avalanche gain mechanism. For many years extensive work has been undertaken to reduce their noise by using engineered multiplication layers that exploit the non-local impact ionization effect[12]–[15]. A common figure of merit when comparing noise performance of APDs is the effective carrier impact ionization ratio (k). McIntyre was the first to use this figure in 1966 when relating the excess noise factor (F) and gain (G) [16] and is based on the statistics of the probabilities of carriers gaining and losing energy subject to high electric fields.

In this paper we use a TCAD model to estimate the excess noise factor and gain and compare the simulated results and with the measured performance results on APDs with a multiplication layer design. This analytical model includes the cases where photons are absorbed in the avalanche region and accurately estimating excess noise factor depending on the absorption profile and the hole-to-electron ionization coefficient (k).

McIntyre [16] derived the expression relating G and F through k:

$$F = k \cdot G + (1 - k) \cdot (2 - 1/G) \qquad (1)$$

where k is the effective ionization rate ratio of holes and electrons.

The gain is defined as:

$$G = I_T / I_p \qquad (2)$$

where I_T is the total photocurrent in the APD given by the difference between the total current in the APD under illumination, and the total current in the APD under dark conditions. Ip, the primary photocurrent, is given by the expression:

$$I_p = q \cdot P \cdot \acute{\eta} . \lambda / (h \cdot c) \qquad (3)$$

where q is the electronic charge, P is the power of optical illumination, $\acute{\eta}$ is the quantum efficiency, λ is the wavelength of illumination, h is the Planck constant, and c is the speed of light. I_p is also the value of I_T when the APD gain is unity. For APD design with separate absorption and multiplication layer heterostructures, it may be difficult to identify the unity-gain point in I_T versus voltage characteristics, making the determination of I_p inaccurate. Sometimes, this value is inferred based on measurements of p-i-n photodiodes with similar layer structures or on the value of optical absorption lengths previously published with assumptions of optical transmission through anti-reflective coatings and different layers of semiconductor materials[17][18]. However, due to uncertainties in layer thicknesses and compositions, each of these methods introduces substantial error in determining the gain. While equation (1) agrees well with the characteristics of conventional APDs with thick multiplication layers, it may not account for non-local effects in the multiplication layer of InGaAs-InP based APDs[12][13]. For APDs made with materials with significant non-local effects in the multiplication layer, the relation more closely follows the expression:

$$F = k_n \cdot G + (1 - k_n) \qquad (4)$$

where k_n is not the same as k in equation (1), but is a similar indirect figure of merit reflective of the noise performance for APDs[17], [19-21]. A Monte-Carlo model results suggest that in these types of APDs the gain distribution function follows a log-normal relationship[19].

One of the features of equation (4) is that it allows the determination of a value for I_p directly, without the need for estimates of quantum efficiency. Combining equation (4) and the equation for excess noise in an APD

$$i^2_n / B = 2 \cdot q \cdot I_p \cdot G^2 \cdot F \qquad (5)$$

where i^2n/B is the noise spectral density, we get the expression

$$i^2_n/(2 \cdot B \cdot I^2_p) = q \cdot k_n \cdot I_T/(I^2_p) + q \cdot (1 - k_n)/(I_p) \quad (6)$$

Thus, from noise spectral density and photocurrent measurements we can plot the left-hand side of equation (6) versus I_T and obtain a linear characteristic with slope

$$A = q \cdot k_n/(I^2_p) \quad (7)$$

and intercept

$$B = q \cdot (1 - k_n)/I_p \quad (8)$$

From (7) and (8) and the quadratic formula one can estimate the values of Ip, k_n, and subsequently values of G, F and ή.

EXPERIMENTAL APD RESULTS

The noise and photocurrent characteristics of InP/InGaAs SWIR APD's with a separate absorption, gain, charge and multiplication layer (SAGCM) epitaxial structure are measured and analyzed. The epitaxial structure and fabrication processes are described elsewhere [22][23]. A schematic cross section of a SWIR APD design is shown in Figure. 1. As shown in Figure 1, the InGaAsP transition layer, the InGaAs absorption layers, and the InP multiplication layer are grown on an InP substrate. To minimize dark current from tunneling, the electric field in the InGaAs absorption layer is kept to less than 150 kV/cm using a thin InP charge layer. A thick, unintentionally doped InP layer is used to reduce the capacitance of the device, while the InGaAsP transition layer eases the transport of holes from the InGaAs absorption layer to the InP multiplication layer. These layers are grown using Metal Organic Chemical Vapor Deposition (MOCVD). The grown wafers are passivated using a plasma enhanced chemical vapor deposited (PECVD) Si_3N_4 dielectric layer. A 'p+' n junction is formed through a diffusion opening in the Si_3N_4 dielectric layer and the depth is controlled through a diffusion process. Metal contacts are then deposited on the anodes and cathodes of the diodes. The metal on the top side also acts as a reflector for the light propagating through the absorption layer for backside-illuminated devices. An antireflective coating is deposited on the polished backside of the wafer.

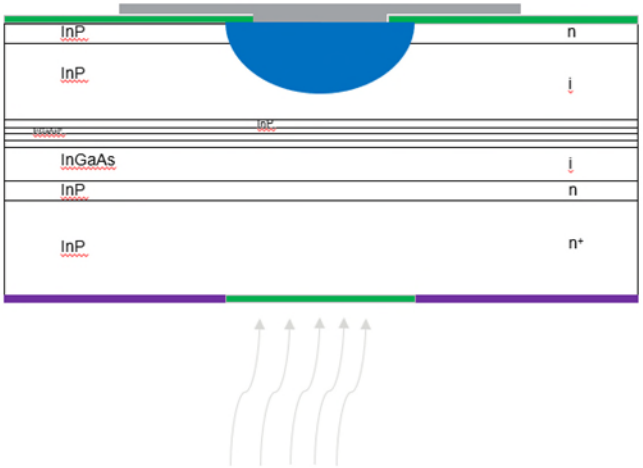

Figure 1. Schematic cross-section of backside-illuminated InP/InGaAs avalanche photodiode.

Figure 2 shows the measured and simulated dark and photo current results of the device design shown in Figure 1. As shown Figure 2, the punchthrough voltage is approximately > 7 V and the breakdown voltage is > 35 V. The measured results confirm the simulation results.

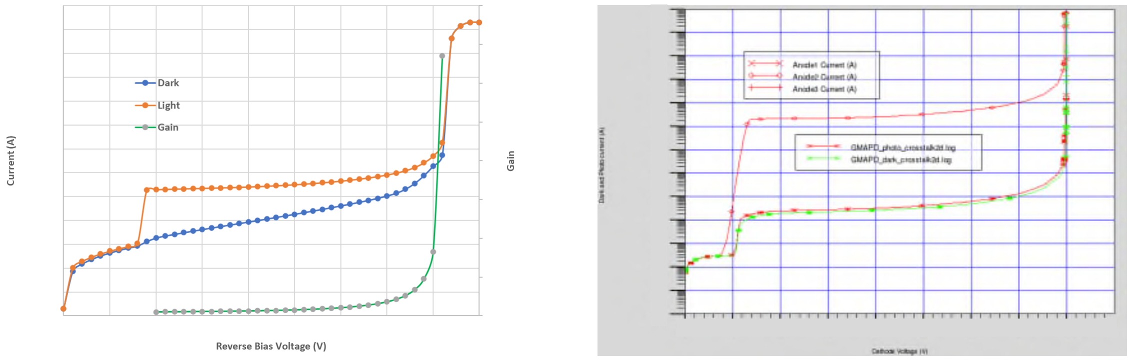

(a). Measurement results (b). Simulation results

Figure 2: Simulated and measured dark and photo current of InP/InGaAs APD

Figure 3 is a schematic test setup to measure dark current, photocurrent, and noise measurement. A stable 1550 nm single-mode, fiber-coupled pulsed laser with varying frequency is used as the optical source. The other end of the fiber is manipulated to align with the active area of the avalanche photodiode. One electrode of the photodiode is connected to a Keithley 2400 source measurement unit to provide the bias and measure the dc current in the photodiode. The other electrode is connected to the input of a low noise oscilloscope. Fast Fourier transforms are performed sequentially on many traces from the oscilloscope and averaged to get a stable and repeatable noise power spectrum.

For the APDs, the noise spectral densities and dc currents are measured as the bias voltage is varied. Measurements are made in both illuminated and dark conditions alternately at each bias voltage. The noise spectral density of the APD due to incident illumination is determined by calculating the difference between noise measured under illumination and noise measured while in the dark, like how the photocurrent is the difference between the measured currents under illumination and dark conditions. The photodiodes selected are of high quality such that the noise measured in the dark is much smaller than while illuminated.

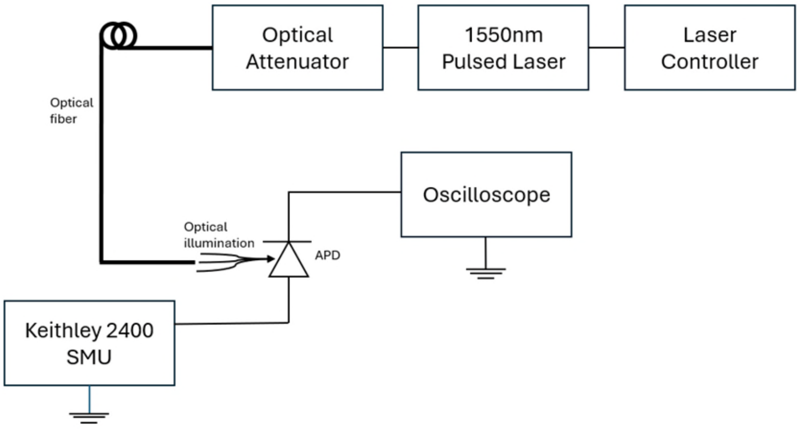

Figure 3: Measurement setup used to measure photodiode photocurrent and noise Vs. bias voltage

Figure 4(a) shows the simulated excess noise factor of electrons and holes in the InP/InGaAs SWIR APD device. As seen in Figure 4, the excess noise factor in the linear mode region of the APD is less than 2 below the breakdown voltage, and in the Geiger mode the noise factor increases exponentially with the gain. Figure 4 (b) shows the measured excess noise factor using the power spectral density measurement method explained above and the results show that the excess noise factor is less than 2 in linear mode and increases exponentially beyond the breakdown voltage as predicted from the simulations. Lower excess noise factor enables longer range spot detection and tracking and increases the range resolution.

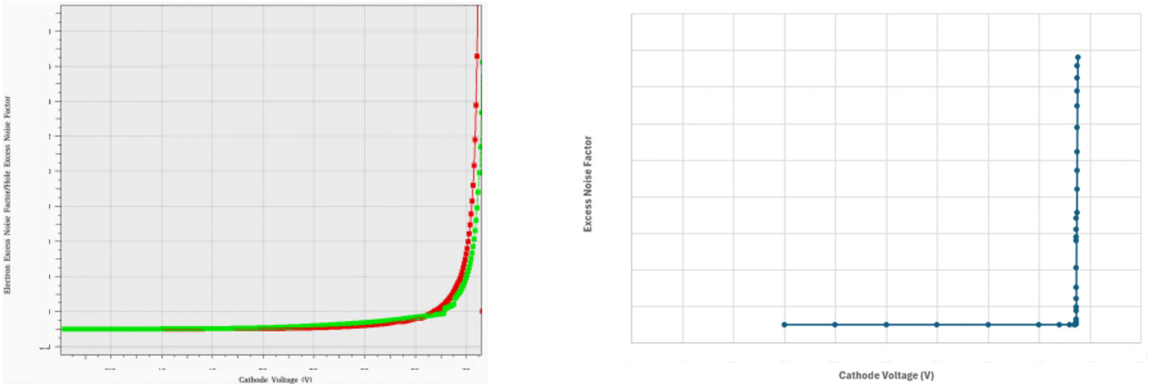

(a) Simulation results (b) Measured results

Figure 4: Simulation and measured results of excess noise factor in SWIR APD

ToF-related Measurements using MMT v4.0 Sensors

Each pixel of the MMT v4.0 sensor supports three distinct modes of operation: low-noise passive imaging, asynchronous laser pulse detection (ALPD), ToF, as well as combinations thereof. Each mode is largely configurable independent of the other modes. For example, in standard MMT mode, the pulse readout path is operated, controlled, and configured almost fully independently from the imaging readout path. The pulse detection readout occurs in a rolling shutter fashion while the imaging channel utilizes a global shutter asynchronous from the pulse variant. Moreover, the pulse detection and imaging data are outputted through a separate, distinct output ports. It is also possible to operate the imaging readout without using the pulse readout, and vice versa. In standard ToF mode, both the imaging and ToF readouts are enabled; however, contrary to standard MMT mode, the readouts are synchronized for calibration purposes. However, the ToF readout can occur with the imaging readout disabled for low-power applications. Pixel level configuration of each operating mode provides several advantages to system-level performance. For instance, it provides the capability to detect pulses of very low power relative to ambient light. Therefore, even if the pulse is not discernable in the pulse channel imagery, which has a higher noise floor as compared to the imaging channel, the pulse can still be detected by the imaging portion of the pixel. One can subsequently make modifications to the pulse channel configuration to detect the pulse in subsequent frames. Since the pulse detection circuit is operating asynchronously from the imaging portion of the pixel, the pulse data can be sampled much more frequently, i.e., at 1 kHz for full frame operation and >20 kHz for sub-window regions, without detriment to the imaging electro-optical performance or power consumption. This allows for detection and decoding of laser designators for target identification in critical and low-SWaP deployments. It is natural for the progression of this technology to include ranging information.

Figure 5 shows the intensity and timestamp (encoded in grayscale) of a received laser pulse from a MMT v4.0 sensor at two different intensity levels separated by ~10X in magnitude. The intensity difference as expected is clearly shown in the right-hand images; the timestamp data is largely unchanged except for the size of the pulse spot. This result is expected as the pulse intensity uniformity is more readily discernable at the lower magnitudes. Figure 6 demonstrates that care also must be taken in the test setup. Although a linear attenuator was utilized, the estimated pulse intensity clearly follows a decaying exponential trend. Therefore, for calibration purposes, this result must be carefully accounted for.

Figure 7 shows the measured pulse sensitivity at ~20 m distance for various sensor pulse sensitivity configurations. Only a portion of entire field-of-view (FoV) is illuminated with a uniform laser pulse. As seen in Figure 7, the pulse is detected both at low and high sensitivity configuration levels. This is paramount for ToF mode. Contrary to ALPD mode where only a small portion of the array is expected to be triggered simultaneously; in ToF mode the entire pixel array could be triggered simultaneously. Pulse detection performance cannot deteriorate, and, clearly, from Figure 7, this was achieved.

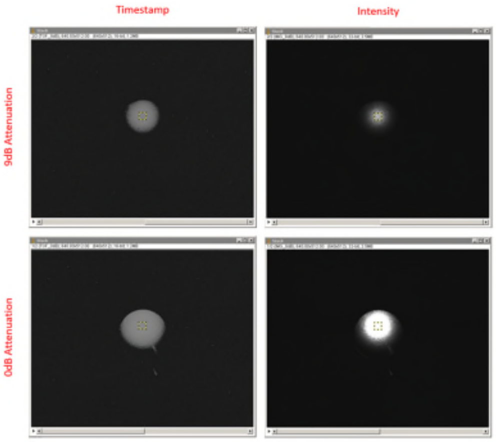

Figure 5: Pulse Intensity and time stamp at two intensity levels

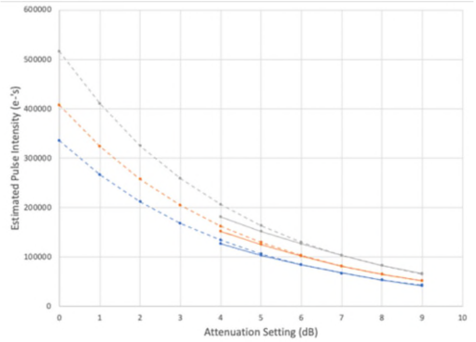

Figure 6: Pulse intensity vs attenuation

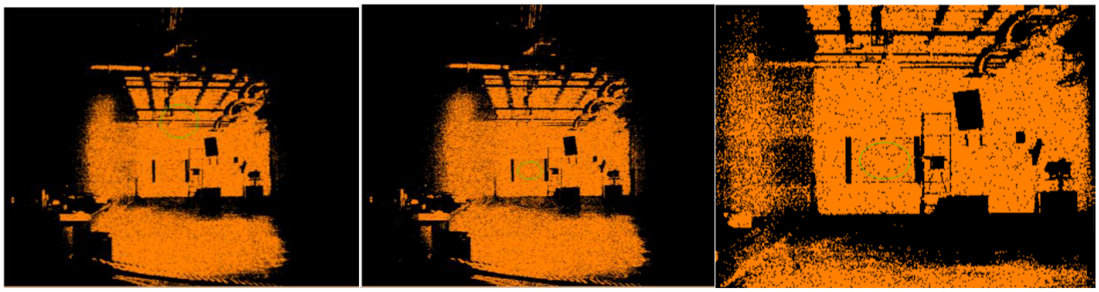

(a) (b) (c)

Figure 7: Pulse detection at a target distance ~20 m at different thresholds (a), (b) with (c) being a zoomed in version of the detection region.

Each variant of MMT camera features simultaneous, full FoV laser pulse detection, tracking, and decoding of up to three laser spots (the sensor itself can detect and track more). For daytime laser spotting, even under high flux conditions, the focal plane maximizes signal collection, using a 99.9% exposure/frame time duty cycle to minimize noise, while capturing pulsed lasers without issue, succeeding even when lasers have slow repetition rates and/or narrow pulse widths (< 10 ns). This novel multi-mode tracking (MMT) capability is borne by the pixel-level laser pulse detection circuit and sensor/camera level processing circuitry. The MMT function enables rapid identification of common battlefield targeting lasers (see-spot), including those with covert eye-safe laser wavelengths, in both day and night conditions. Figure 8 shows three pulses simultaneously detected at 1 kHz pulse frame rates, decoded and tracked at up to 20 kHz pulse frame rates and superimposed on an image frame operating at 30 Hz using the same SUI sensor technology.

Figure 8: Low noise imaging (30fps) and the in-situ pulse detection of 3 separate laser sources using the same SUI MMT camera.

Spot tracking using MMT eSWIR sensors

SUI has designed, developed, and manufactured extended wavelength PiN FPAs in both linear and 2-D formats over the recent decades[24]. The eSWIR photo-detector design and fabrication processes are based on the InP/InAsP/InGaAs material system is utilized widely in the industry[24]. Recent developments include the development of a MMT 2D variant using a 2.2 μm cut-off detector material. Figure 9 shows the 2.0 μm laser pulse detection measurement results at -38 °C and +70 °C FPA temperatures. As seen from Figure 9, the pulse code is detected at higher FPA temperatures as well as at low temperatures. At the higher FPA temperature the image pixels are saturated because of high dark current, as expected at this temperature.

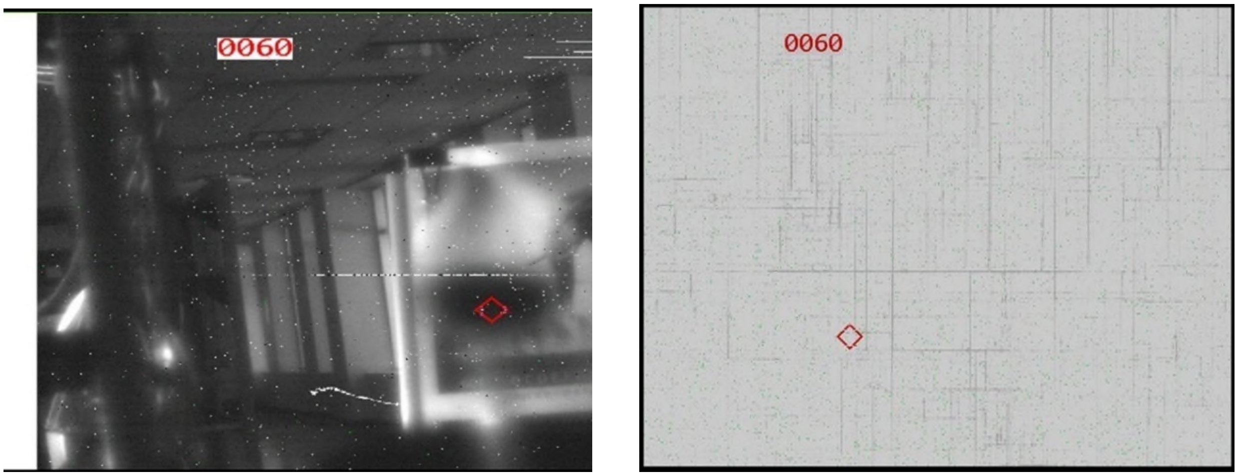

Figure 9: Detection of a 2.0 µm wavelength laser pulse using a SUI MMT eSWIR sensor at a FPA temperature of -38 °C (left) and 70 °C (right), respectively.

CONCLUSION

This work summarizes recent progress in SUI's MMT technology development for laser spot tracking at SWIR and eSWIR wavelengths. Initial results of 640 x 512 MMT FPAs for imaging, pulse detection, and ToF capabilities at SWIR and eSWIR wavelengths have been presented. Also presented were the excess noise factor analysis, simulation, and measured results of next generation MMT FPAs using an APD pixel sensor to enhance the detection and tracking range capability. Immediate next steps in this program are continued improvement in eSWIR pulse tracking, the development of internal gain, low noise APD FPAs, and development of a multi-mode camera featuring a 2K x 2K format FPAs at 10 µm pitch.

ACKNOWLEDGEMENTS

The authors wish to recognize and thank all who contributed to the development of this technology over the years whose names, although not explicitly included here, were instrumental in bringing this work to fruition. We would also like to recognize RTX leadership who entrusted the usage of internal funding to facilitate the work presented.

REFERENCES

1. Y. Arslan, F. Oguz, C. Besikci "Extended wavelength SWIR InGaAs focal plane array: Characteristics and limitations", Infrared Physics & Technology, Volume 70, 2015, Pages 134-137, ISSN 1350-4495, https://doi.org/10.1016/j.infrared.2014.10.012
2. P. Mushini, W. Huang, M. Morales, R. Brubaker, T. Nguyen, M. Dobies, W. Zhang, W. Gustus, G. Mathews, S. Endicter, and N. Paik "2D SWIR image sensor with extended wavelength cutoff of 2.5 µm on InP/InGaAs epitaxial wafers with graded buffer layers", Proc. SPIE 9819, Infrared Technology and Applications XLII, 98190D (20 May 2016); https://doi.org/10.1117/12.2225109
3. K. Linga, J. Liobe, M. Evans, W. Huang, P. Bereznycky, S. Endicter, W. Gustus, R. Cue, J. Tagle, and S. Houlihan "Advanced SWIR APDs for multimode applications", Proc. SPIE 12534, Infrared Technology and Applications XLIX, 1253408 (13 June 2023); https://doi.org/10.1117/12.2664028

4. J. Liobe and D. Malchow "Advancements in multi-mode ROIC design for SWIR detectors (Conference Presentation)", Proc. SPIE 11407, Infrared Technology and Applications XLVI, 114070B (5 May 2020); https://doi.org/10.1117/12.2560707
5. P. A. Forrester and K. F. Hulme, “Laser rangefinders,” Optical and Quantum Electronics, vol. 13, pp. 259-293, July 1981.
6. US9948880B2 – "Asynchronous multimode focal plane array,” 2016.
7. US10520589B2 – “Pixel output processing circuit with laser range finding (LRF) capability,” 2017.
8. US9641781B2 – “Imaging circuit including frame asynchronous pulse detection,” 2015.
9. A. Patadia, S. Baliga, D. Babic, "Extended InGaAs PIN photodiode with improved linearity for FTIR spectroscopy," Proc. SPIE 12893, Photonic Instrumentation Engineering XI, 128930K (11 March 2024); https://doi.org/10.1117/12.3003366
10. A. Dehzangi, J. Li, M. Razeghi, “Low Noise Short Wavelength Infrared Avalanche Photodetector Using SB-Based Strained Layer Superlattice”, Photonics. 2021; 8(5):148. https://doi.org/10.3390/photonics8050148
11. B. Guo, M. Schwartz, S. H. Kodati, K. M. McNicholas, H. Jung, S. Lee, J. Konowitch, D. Chen, J. Bai, X. Guo, T. J. Ronningen, C. H. Grein, J. C. Campbell, S. Krishna, “InGaAs/AlInAsSb avalanche photodiodes with low noise and strong temperature stability”, APL Photonics 1 November 2023; 8 (11): 116112. https://doi.org/10.1063/5.0168134
12. R. J. McIntyre, “A new look at impact ionization—Part I: A theory of gain, noise, breakdown probability, and frequency response,” IEEE Trans. Electron Dev., vol. 46, no. 8, pp. 1623–1631, Aug. 1999.
13. P. Yuan, K. A. Anselm, C. Hu, H. Nie, C. Lenox, A. L. Holmes, B.G. Streetman, J. C. Campbell, and R. J. McIntyre, “A new look at impact ionization—Part II: Gain and noise in short avalanche photodiodes,” IEEE Trans. Electron Dev., vol. 46, no. 8, pp. 1632–1639, Aug. 1999.
14. J. C. Campbell, “Recent advances in telecommunications avalanche photodiodes,” J. Lightw. Technol., vol. 25, no. 1, pp. 109–121, Jan. 2007.
15. W. R. Clark, K. Vaccaro, and W. D. Waters, “InAlAs-InGaAs based avalanche photodiodes for next generation eye-safe optical receivers,” Proc. SPIE, vol. 6796, p. 67962H, 2007.
16. R. J. McIntyre, “Multiplication noise in uniform avalanche diodes,” IEEE Trans. Electron. Dev., vol. ED-13, no. 1 pp. 164–168, Jan. 1966.
17. N. Duan, S. Wang, F. Ma, N. Li, J. C. Campbell, C. Wang, and L. A. Coldren, “High speed and low-noise SACM avalanche photodiodes with an impact-ionization engineered multiplication region,” IEEE Photon Technol. Lett., vol. 17, no. 8, pp. 1719–1721, Aug. 2005.
18. W. R. Clark, A. Davis, M. Roland, and K. Vaccaro, A 1 cm × 1 cm In0.53Ga0.47 As-In0.52 Al0.48 As avalanche photodiode array,” IEEE Photon. Technol. Lett., vol. 18, no. 1, pp. 19–21, Jan. 2006.
19. W. Sun, X. Zheng, and J. C. Campbell, “Study of excess noise factor under non-local effect in avalanche photodiodes,” IEEE Photon. Technol. Lett., vol. 26, no. 21, pp. 2150–2153, Nov. 1, 2014.
20. W. R. Clark, A. Margittai, J. -P. Noel, S. Jatar, H. Kim, E. Jamroz, G. Knight, and D. Thomas, “Reliable, high gain-bandwidth product InGaAs/InP avalanche photodiodes for 10 Gb/s receivers,” in Proc. Opt. Fiber Commun. Conf., Int. Conf. Integr. Opt. Opt. Fiber Commun. Techn. Dig., Feb. 1999, vol. 1, pp. 96–98.
21. W. Sun, X. Zheng, Z. Lu, and J. C. Campbell, “Monte Carlo simulation of InAlAs/InAlGaAs tandem avalanche photodiodes,” IEEE J. Quantum Electron., vol. 48, no. 4, pp. 528–532, Apr. 2012.
22. K. Linga, J. Liobe, M. Evans, W. Huang, P. Bereznycky, S. Endicter, W. Gustus, R. Cue, J. Tagle and S. Houlihan, “Advanced SWIR APDs for Multimode Applications”, Proc. SPIE Volume 12534, Infrared Technology and Applications XLIX; 1253408 (2023) https://doi.org/10.1117/12.2664028
23. K. Linga, W. Huang, B. Gustus, J. Chi and J. Liobe, “Advanced SWIR sensor development at SUI”, Proc. SPIE Volume 13046, Infrared Technology and Applications L; 1304602 (2024) https://doi.org/10.1117/12.3013852
24. P. Mushini, W. Huang, M. Morales, R. Brubaker, T. Nguyen, M. Dobies, W. Zhang, W. Gustus, G. Mathews, S. Endicter and N. Paik, “2D SWIR Image sensor with extended wavelength cutoff of 2.5 μm on InP/InGaAs epitaxial wafers with graded buffer layers”, Proc. SPIE 9819, Infrared Technology and Applications XLII, 98190D (20 May 2016); https://doi.org/10.1117/12.2225109